Four-Port Wide-Band Cavity-Backed Antenna with Isolating X-Shaped Block for Sub-6 GHz 5G Indoor Base Stations

JAIME MOLINS-BENLLIURE (ID),
EVA ANTONINO-DAVIU (ID), **(Member, IEEE)** ,
MARTA CABEDO-FABRÉS (ID), **(Member, IEEE) and**
MIGUEL FERRANDO-BATALLER (ID), **(Life Member, IEEE)**

Instituto de Telecomunicaciones y Aplicacionens Multimedia (iTEAM), Universitat Politècnica de València. C/ Camí de Vera s/n 46022 València (Spain).

Corresponding author: Jaime Molins-Benlliure (e-mail: jaimoben@iteam.upv.es).

ABSTRACT A four-port wideband cavity-backed antenna is presented for indoor base stations applications. The antenna is composed of a square open cavity with an X-shaped isolating block and 4 feeding monopoles symmetrically and orthogonally arranged in the aperture of the cavity. A novel methodology based on Characteristic Modes Analysis (CMA) is used for identifying the modes which are contributing to the coupling. As a result of this analysis, an X-shaped isolating block placed at the center of the cavity is proposed for increasing the isolation between ports. A wide-band four-port antenna with unidirectional radiation patterns is obtained with a measured impedance bandwidth (S_{11}<-10 dB) ranging from 1.55 to 6 GHz (118%), covering most of the sub-6 GHz 5G bands. The proposed antenna provides four independent radiation patterns, with 16 dB of measured minimum isolation between ports and an efficiency higher than 84%. Multiple-input multiple-output (MIMO) compatibility is confirmed with a 4×4 MIMO simulated system with an envelope correlation coefficient (ECC)<0.5 in different propagation conditions. The antenna is easy to fabricate and presents a compact size of 129.5×129.5×28.2 mm^3 ($0.68\lambda \times 0.68\lambda \times 0.15\lambda$, at a frequency f=f$_{min}$=1.55 GHz). Moreover, the antenna has the advantage of avoiding complex feeding structures with baluns or directional couplers.

INDEX TERMS Cavity-Backed antenna, Characteristic Modes, Indoor Base Station, MIMO, 5G, Sub-6 GHz.

I. INTRODUCTION

THE arrival of the new 5G wireless communication system emerges as the solution for providing connectivity to an enormous number of terminals, meeting the new requirements regarding data rate, latency, efficiency and reliability [1]. The early deployment of the 5G will be supported by the so-called sub-6 GHz bands which have the advantage of the retro-compatibility with the current infrastructure deployed for the previous wireless systems.

Currently, there is a growing demand for 5G indoor base station antennas covering the new licensed sub-6 GHz bands and also the 2G/3G/4G bands, which are still working. Most existing solutions are based on wide-band or multi-resonant (multi-band) structures, providing single or dual-polarized antennas. The requirements for these antennas are unidirec-

tional radiation patterns, high total efficiency and decoupled ports. Moreover, low-profile, easy-manufacturing and low-cost are also very appreciated characteristics for an easy and rapid installation of the antennas in indoor scenarios.

Recent papers propose multi-band antenna solutions consisting of a triple-band and dual-polarization radiating structure based on crossed dipoles [2], a compact single-port quadruple-band antenna that combines an asymmetrical dipole and parasitic patches [3], and a low-profile dual-band dual-polarized antenna, with an artificial magnetic reflector [4]. Regarding wide-band solutions, a single-port solution based on a dual-sleeve monopole is proposed in [5] and a three-port antenna is presented in [6], which uses the novel tri-polarized antenna concept and the combination of

a monopole-equivalent structure and two orthogonal stepped dipoles.

In addition, multiple-input multiple-output (MIMO) capability is a highly demanded characteristic for increasing the data rate in 5G indoor base stations. MIMO operation requires multiple port antennas with highly isolated ports and independent radiation patterns with a low Envelope Correlation Coefficient (ECC) between them. A compact dual-broadband (0.8-0.9 GHz, 1.7-2.7 GHz) MIMO antenna composed by a microstrip patch with slots and two monopoles for 2G/3G/4G/5G systems is presented in [7]. In addition, a four-port wide-band annular-ring patch antenna has recently been proposed in [8], working at 3.3-5 GHz band. In a previous work, the authors of this paper presented a MIMO antenna with 4 independent ports, but with a low isolation between them [9].

The isolation between ports is a critical parameter, specially when multiple-port solutions are mounted in limited space scenarios. Some of the techniques used for increasing isolation are based on using a decoupling element [10], a neutralization line [11], orthogonal polarizations [12]- [17], decoupling networks [18] and self-isolated/self-decoupled [19]- [21] antennas. In addition, the interest on Characteristic Modes Analysis (CMA) in modern applications [22] has increased due to the possibility of exciting different orthogonal modes on a radiating ground plane of a hand-held device for MIMO compatibility. CMA has been applied to several planar solutions that have been proposed for MIMO systems covering different bands with low coupling [23]- [26].

In this paper, a four-port wide-band cavity-backed antenna is proposed for sub-6 GHz 5G indoor base station applications. The design consists of 4 T-shaped monopoles arranged in an orthogonal and symmetric configuration. An X-shaped isolating block is included at the center of the cavity to increase the isolation between ports. The design provides four independent unidirectional radiation patterns with high efficiency, MIMO capability and a wide-band impedance bandwidth. Due to the presence of the isolating block, it is not necessary to use differential feeding to isolate the ports, what would decrease the number of independent ports. Thus, hybrid couplers or baluns are note required here, turning the design into an easy-manufacturing and low-cost solution, suitable for being installed as an indoor MIMO base station antenna.

The novelty of the paper lies in the characteristic modes based methodology used to obtain a four-port wide-band design by exciting clusters of orthogonal modes and identifying which of them contribute to the coupling between ports. With this information, a proper isolating element (isolating block) is introduced to fade the non-desired modes. As a result of the inclusion of an isolating block, the coupling between ports is reduced to the minimum required for base station indoor applications, obtaining a four-port decoupled design which improves the performance of some antennas proposed in recent publications like [8]. Unlike the referenced designs based on characteristic modes which try to excite a single

mode per independent port, either using direct feeding or differential feeding, in the proposed design each independent port excites a cluster of modes, which provides the wide-band behaviour of the antenna. In addition, all the referenced designs are not 3D, but planar designs based on simple structures. In the proposed design, characteristic modes are applied for the first time for analyzing an open cavity fed by monopoles, which is a 3D structure that involves high complexity.

The paper is organized as follows: In Section II, the initial design is presented, showing the limitations in terms of coupling. In Section III, a characteristic modes analysis is applied to the initial design for the understanding of the antenna performance and the identification of the modes which are contributing to the coupling between ports. In Section IV, a novel decoupling methodology based on the characteristic modes analysis is presented to minimize the excitation of the modes which are contributing to the coupling with the use of an isolating block and the geometry of the final design is presented. In Section V, a comparison between different isolating block geometries is detailed. In Section VI, the results of the simulated and measured final design are presented. In Section VII, the performance of the proposed antenna is evaluated in a 4×4 MIMO system under different propagation conditions. Finally, Section VIII exposes the conclusion of the paper.

II. INITIAL DESIGN

Our initial approach to design a wide-band and unidirectional structure is based on the combination of wide-band elements. As shown in Fig. 1(b), the first element is a squared cavity that may exhibit unidirectional and wide-band behaviour if properly excited. Taking advantage of the symmetry of this cavity, 4 independent feeding elements are placed in a symmetric and orthogonal arrangement in the middle of the four edges at the top aperture of the cavity (see Fig. 1(b)).

A wide-band excitation is necessary to attain a wide-band operation of the cavity. Therefore, T-shaped planar monopoles (shown in Fig. 1(a)) have been chosen for the design, since they are easy to construct and they present large impedance bandwidth.

The minimum operating frequency is determined by the length l_m (Fig. 1(a)) of the monopoles, since $l_m = \lambda/4$ at $f=f_{min}$. In addition, a minimum separation of $\lambda/2$ ($f=f_{min}$) is required between feedings to guarantee minimum coupling. In this case, four feedings (monopoles) have been incorporated, resulting in a minimum square cavity aperture perimeter of 2λ.

Taking these considerations into account, the dimensions of the antenna have been optimized to operate in the sub-6 GHz 5G bands. The final dimensions of the structure are summarized in Table 1, resulting an antenna with total electrical size of $0.68\lambda \times 0.68\lambda \times 0.15\lambda$ (at $f=f_{min}$).

Fig. 1(c) shows the simulated S-parameters of this initial antenna. As observed, this cavity is a promising four-port wide-band solution with the drawback of low isolation be-
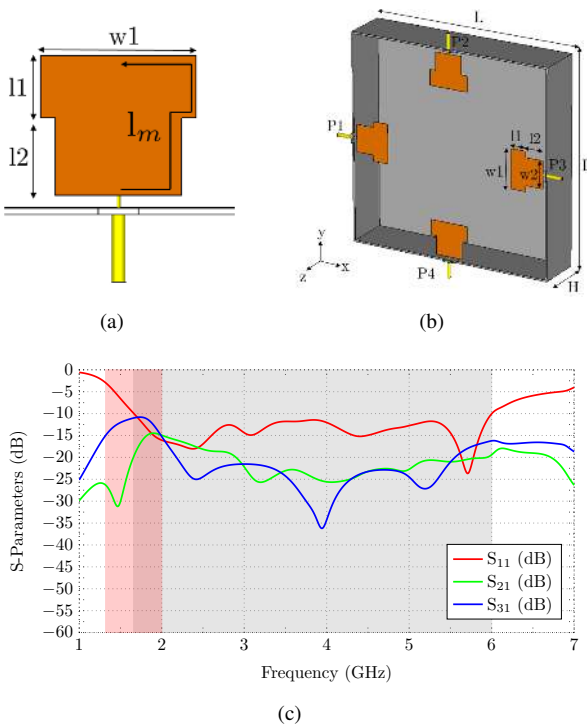
FIGURE 1: a) T-shaped monopole; b) Initial design with the squared cavity; c) S-Parameters of the initial design, where $S_{21}=S_{41}$ and $S_{31}=S_{42}$. Note that red area highlights the band with high coupling levels (from 1.35 to 2 GHz), whereas grey area shows the operating bandwidth (from 1.55 to 6 GHz). Dimensions are detailed in Table 1.

TABLE 1: Dimensions of the initial design (unit: mm)

L	H	w1	w2	l1	l2
130.5	29.2	24	18.5	9.5	11.5

tween ports, specially between adjacent ports P1 and P2 at 1.35-2 GHz (see red area and S_{21} in Fig. 1(c)). This isolation is not high enough for the antenna to be installed in an indoor base station. Consequently, a modal analysis using TCM is going to be performed next, in order to get insight into the reason for the high coupling between ports and overcome the problem. Notice that the minimum matched frequency is f_{min}=1.55 GHz, hence the analysis will be focused at 1.55-2 GHz, which is the band with coupling issues in the operating impedance bandwidth.

III. MODAL ANALYSIS OF AN OPEN CAVITY

The electromagnetic analysis of a closed square cavity is well known and described in the electromagnetic theory with field cavity modes. In an open cavity, the information is not detailed and the inclusion of the feeding elements would not be considered in a cavity modes analysis. For the proper understanding, we propose the use of characteristic modes analysis, which is an appropriate approach to analyze an open

cavity including the four monopoles.

The Theory of Characteristic Modes (TCM) [27]- [28] provides a basis set of currents on a structure with an arbitrary geometry, which exhibits orthogonal radiation properties. It provides a physical interpretation of the radiating mechanisms of the structure and helps to determine the optimum feeding configuration. Characteristic modes are obtained from the following eigenvalue problem that is solved using the Method of Moments (MoM):

$$[X]\vec{J}_n = \lambda_n[R]\vec{J}_n \qquad (1)$$

where $\vec{J}_n$ is the n_{th} real eigenvector (characteristic current) and λ_n is the n_{th} eigenvalue. [X] and [R] correspond to the imaginary and real parts of the complex generalized impedance matrix of the structure [Z], respectively. In addition, the surface current density can be expressed as follows:

$$\vec{J} = \sum_n \alpha_n \vec{J}_n = \sum_n \frac{V_n^i}{(1+j\lambda_n)}\vec{J}_n \qquad (2)$$

where α_n describes the modal weighting coefficient (MWC) and V_n^i the modal excitation coefficient (MEC). Eigenvalues (λ_n) depend on the frequency and give information about the resonance of the associated current mode. The mode is at resonance when λ_n=0. When λ_n is negative, the mode stores electric energy, whereas when λ_n is positive the stored energy is magnetic. There are different modal attributes for the physical interpretation of the eigenvalues [29]. In this paper, the characteristic angle (α_n) is chosen for the analysis, and it is derived as follows:

$$\alpha_n = 180° - \tan^{-1}(\lambda_n) \qquad (3)$$

As stated above, when the mode is at resonance $\lambda_n = 0$, and hence $\alpha_n = 180°$.

For a proper understanding, and due to the complexity of the structure, the modal analysis of the 3D structure is limited to the frequency range from 1.1 to 2.1 GHz, considering only the lowest order characteristic modes, and including the band from 1.55-2 GHz which has coupling issues. Nevertheless, the identification of the first resonant modes at low frequencies helps to understand the behaviour of the antenna at higher frequencies.

Fig. 2(a) depicts the characteristic angle variation with frequency for the first resonant modes (J_n) of the initial design (solid lines) described in Fig. 1, which dimensions correspond with those of Table 1. Since J_1 and J_2 are degenerated modes, only the characteristic angle of J_1 is presented. As observed, all the analyzed modes resonate below 2 GHz. Fig. 3 shows the current distribution and the electric near field distribution associated to each mode at resonance. J_1 (Fig. 3(a)) and J_2 (Fig. 3(c)) are the horizontal and vertical fundamental modes, J_3 (Fig. 3(e)) is a mode with current nulls in the corners of the cavity and with current maximum at the center of the outer walls of the cavity. As observed, its electric field distribution E_3 (Fig. 3(f)) has a maximum at the corner of the cavities and a null at the center. J_4 (Fig. 3(g))
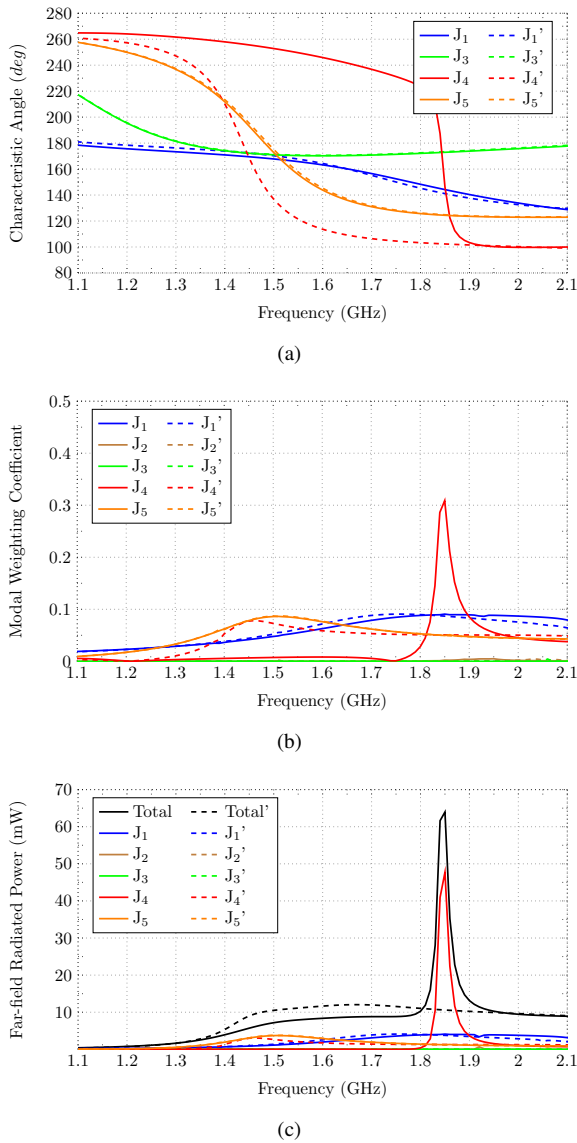
FIGURE 2: a) Characteristic angle of the initial design (solid curves) and final design (dashed curves); b) Modal Weighting Coefficient of the initial design (solid curves) and final design (dashed curves); c) Far-field power contribution of the initial design (solid curves) and final design (dashed curves).

is a radial mode, in which the currents flow from the center of the cavity to the four monopoles and E_4 (Fig. 3(h)) has a maximum in the center of the cavity, with perpendicular direction. J_5 (Fig. 3(i)) has a distribution similar to that of J_3 but in this case the current nulls are in the center of the outer walls and not in the corners. E_5 exhibits a maximum where the monopoles are located and a minimum in the center of the cavity. Regarding the electric field distribution of the modes, as can be observed, all of them have a TE distribution except E_4, which has a TM field distribution.

Since a capacitive feeding is used in the proposed design, only modes with maximum field at the feeding position
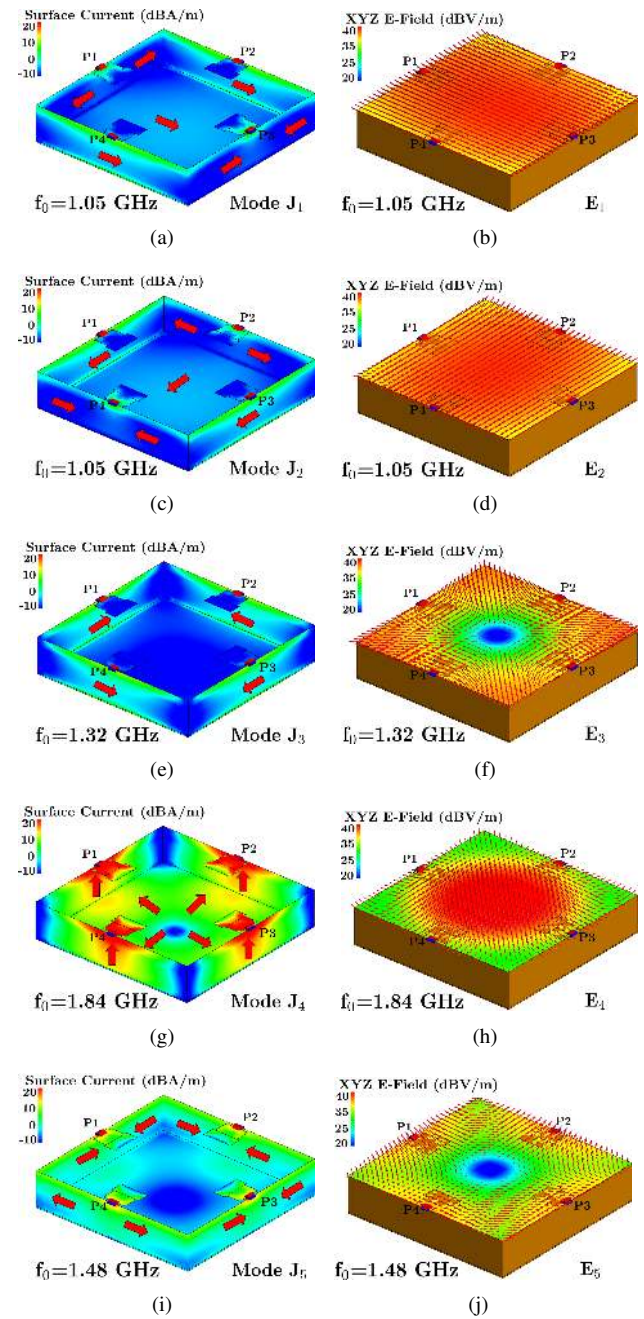

FIGURE 3: Instantaneous magnitude of the modal current distribution J_n and modal field distribution E_n at modal resonance f_0 of the initial design: a) J_1; b) E_1; c) J_2; d) E_2; e) J_3; f) E_3; g) J_4; h) E_4; i) J_5 and j) E_5.

will couple to the excitation. Fig. 2(b) and Fig. 2(c) present the Modal Weighting Coefficient (MWC) and the far-field power contribution obtained when port P1 is excited, respectively. It should be noted that both parameters depend on the excitation, but the MWC does not take into account the port impedance matching. From these two figures it can be extracted that when port P1 (or port P3) is active, only modes
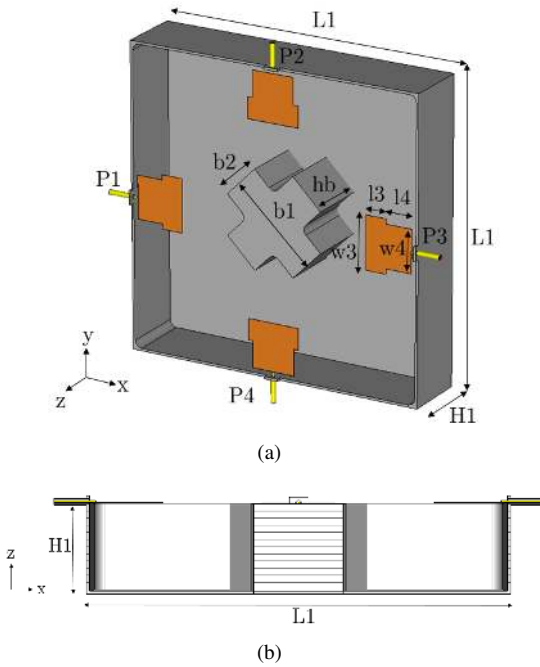
(a)

(b)

FIGURE 4: a) Overall view of the antenna including the four monopoles coloured in orange and the square open cavity with the X-shaped block coloured in grey. b) Side view of the design (XZ-plane). Dimensions are detailed in Table 2.

TABLE 2: Dimensions of the final design (unit: mm)

L1	H1	w3	w4	l3	l4	b1	b2	hb
129.5	28.2	23.15	18.7	9.3	11.5	42.6	17.8	26.6

J_1, J_4 and J_5 are excited. Due to the symmetry, when port P2 (or port P4) is active, only modes J_2, J_4 and J_5 will contribute to the total radiated power. Mode J_3 is not excited in any case because it has a current maximum and minimum electric field at the feeding locations, so it does not couple with the feeding monopoles.

It is also observed that below 1.8 GHz there is no dominant mode, but once mode J_4 resonates (at 1.84 GHz), it becomes dominant, making a great contribution to the total radiated power. In Fig. 1(c) it is detailed that the maximum coupling between ports P1 and P2 occurs exactly when mode J_4 resonates. These results reveal that the low isolation between adjacent ports from 1.55 to 2 GHz is due to the excitation of the radial current mode J_4.

The following section details a novel methodology based on CMA that is used to improve the isolation between ports of this initial design.

IV. DECOUPLING METHODOLOGY

The initial design presents low isolation between adjacent ports in the frequency range between 1.55 and 2 GHz. At this stage, a full-wave analysis does not provide clear information about the coupling, because the total currents and total fields
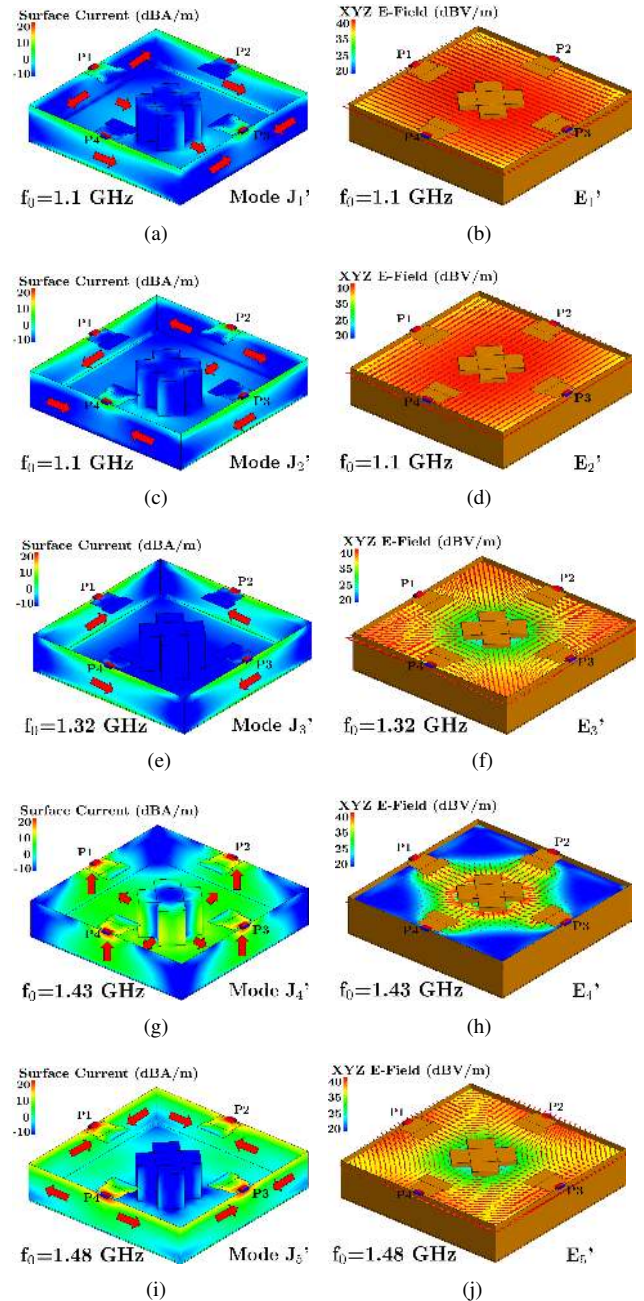

FIGURE 5: Modal current distribution J_n' and modal field distribution E_n' of the initial design at modal resonance f_0' . Instantaneous magnitude: a) J_1', b) E_1', c) J_2', d) E_2', e) J_3', f) E_3', g) J_4', h) E_4', i) J_5' and j) E_5'

are a combination of several modes so it is difficult to identify the reason for the coupling. In section III, CMA has been applied to identify the modes of the square cavity that are excited when one of the feeding monopoles is activated. The goal of this section is to use CMA to identify which modes are causing the coupling between ports already observed. The modal analysis reveals that a decoupling structure placed in the centre of the cavity is a good solution for fading the non-

desired modes.

As demonstrated before, the far-field radiated power from 1.55 to 2 GHz obtained when port P1 is excited, is mainly produced by modes J_1 and J_4 (Fig 2(c)). The current distribution of Mode J_1 (Fig. 3(a)) shows that the currents associated to this mode flow from port P1 to port P3. Since this current flow is orthogonal to ports P2 and P4, it can be concluded that mode J_1 is not responsible of the high coupling observed between adjacent ports. In contrast, mode J_4 has maximum contribution to radiation at the frequency in which the coupling between ports P1 and P2 is maximum (Fig 1(c)). Moreover, the current distribution of mode J_4 (Fig. 3(g) shows that this mode has minimum current at the center of the cavity and the currents flow radially towards the four monopoles. The current intensity associated to mode J_4 is high inside the cavity and all the ports have intense induced currents, which turns into coupling between ports.

Therefore, the modal analysis reveals that mode J_4 is responsible for the high coupling between adjacent ports at these frequencies.

As seen in Fig. 3(h), the electric field flows in the z-axis direction and exhibits a maximum in the center of the cavity. Mode J_4 has no variation in the z-axis and the maximum magnitude is settled in the center. The solution taken to mitigate this mode is to place a metallic block in the center of the cavity. A metallic block placed in the center cancels the electric field in z-direction, changing the boundary conditions of the cavity. The final design is described in Fig. 4 and its dimensions detailed in Table 2. In this new scenario, the electric field distribution E_4 of mode J_4 cannot exist.

Different block shapes have been analyzed (section V). All of them vanish mode J_4, but some geometries have different impact on the other modes. The goal is to fade mode J_4 and not to disturb the rest of modes. The chosen geometry is the X-shaped block and in the following section will be justified.

To verify this effect, the modal analysis of the final design including the isolating block is presented in Fig. 5. The notation of J_n and J_n' is used for representing the modes of the initial design without isolating block (J_n) and the modes of the final design with the isolating block (J_n'). As observed in Fig. 4, the characteristic currents and characteristic electric fields have an identical distribution of those in Fig. 3 (structure without block), with the exception of mode J_4'.

In Fig. 2 the characteristic angle and the far-field radiated power are depicted for the initial design (without block) and for the final block (with block), at the analyzed band with coupling issues (1.55-2 GHz). Modes J_1, J_2 and J_3 are not distorted by the inclusion of the block (see J_1', J_2' and J_3' in Fig. 2(a)). However, J_4 is shifted to lower frequencies (see J_4') and the peak power at 1.85 GHz fades due to the presence of the isolating block, as desired. As mentioned above, the mode J_4 vanishes due to the inclusion of the isolating block, but it still appears at the characteristic angle representation (J_4'), resonating at 1.45 GHz and having some power contribution at resonance. The reason behind this phenomenon can be explained with the field representation
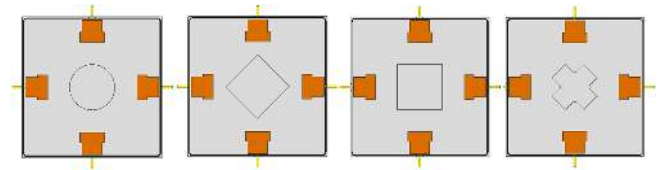

FIGURE 6: The four analyzed designs with different isolating-block geometries: circular, rhombus, square and X-shaped.

of the mode J_4'. Fig. 5(h) illustrates the modal electric field distribution of mode J_4' at the aperture. Its electric field distribution has no component in the z-axis showing a TEM-like field distribution.

In conclusion, the mode J_4 is responsible for the coupling in the initial design. In order to improve the behavior, an isolating block is used to vanish mode J_4 and a new J_4' mode appears when the modes of the final design are computed. J_4' mode represents a new mode created by the inclusion of the inner block. The new J_4' mode has no impact on the coupling because its electric and magnetic fields are maximum in the center of the cavity surrounding the isolating block.

V. ISOLATING BLOCK GEOMETRIES

In this section a comparison of four different isolating-block geometries is presented in terms of coupling and matching. Figure 6 shows the four geometries, including the circular, the rhombus, the square and the X-shaped blocks.

As stated in the previous section, the goal of the isolating block is to vanish mode J_4' for increasing the isolation between ports, and at the same time not to distort the modes which are contributing to the wide-band performance of the antenna.

Fig. 7(a) depicts the S_{11} parameter of all the geometries. The X-shaped geometry has an excellent behaviour with $S_{11} <$-10 dB in a wide range of frequencies. The circular geometry has matching issues between 5 and 5.4 GHz, the square geometry at 3.5 GHz and 3.9 GHz and the rhombus geometry at 5 GHz.

The coupling between ports P1 and P2 can be determined by the S_{21} parameter depicted in Fig. 7(b). X-shaped and square block geometries show a good performance with coupling lower than $S_{21} <$-15 dB in the analyzed frequency range. The circular case has coupling issues at 3.3 GHz and the rhombus between 4.4-4.7 GHz.

The last analyzed parameter in Fig. 7(c) is the coupling between ports P1 and P3 (S_{31}). X-shaped and circular block geometries present coupling levels lower than $S_{31} <$-15 dB.

	Circular	Rhombus	Square	X-Shaped
$S_{11} <$-10 dB	✗	✗	✗	✓
$S_{21} <$-15 dB	✗	✗	✓	✓
$S_{31} <$-15 dB	✓	✗	✗	✓

TABLE 3: Comparison table between isolating block geometries.

IEEE *Access*

(a)

(b)

(c)

(d)

FIGURE 8: a) Fabricated Antenna b) Dissembled antenna c) Antenna set-up for the measurement with the network analyzer and, d) Antenna set-up for the measurement in the anechoic chamber.
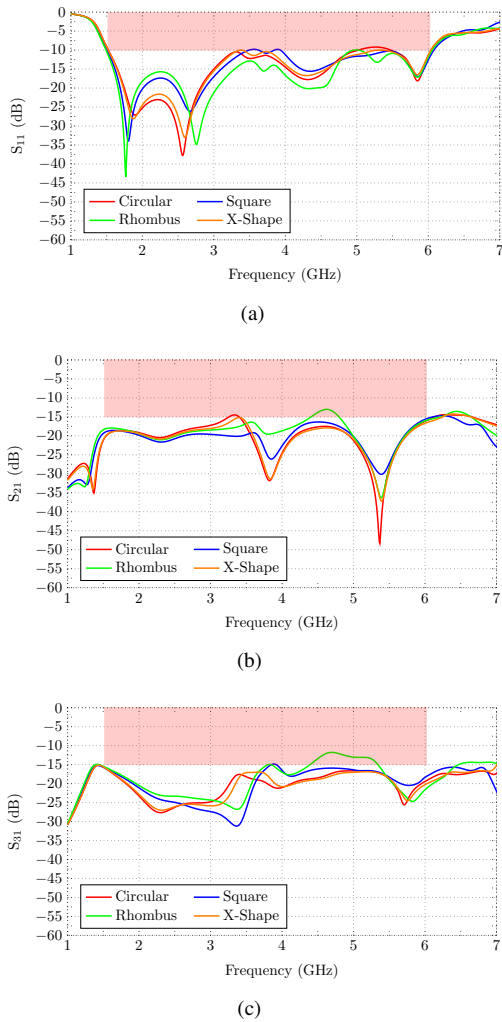

FIGURE 7: a) S_{11} of the four analyzed designs, b) S_{21} of the four analyzed designs and c) S_{31} of the four analyzed designs. Red area (values in the impedance bandwidth from 1.55 to 6 GHz in which minimum matching(S_{11}) or coupling (S_{21}, S_{31}) is not satisfied)

FIGURE 9: S-parameters of the final design. Due to the design symmetry, S_{21}=S_{41}.

The rhombus has coupling issues at 4.4-5.3 GHz and the square at 3.9 GHz.

Table 3 summarizes the results obtained in the analysis. The X-shaped geometry is the most suitable one due to the results obtained throughout the entire band. The physical reason behind these results can be addressed with the size and geometry of the X-shaped block. The X-shaped block has a geometry which is able to vanish mode J_4 with lower size than the rest of the blocks, hence, it is more innocuous to the rest of modes which flow through the edges of the cavity. It does not interfere into matching and does not induce coupling due to its lower size. In addition, the X-shaped block has not parallel sides to the monopoles which would induce more coupling.
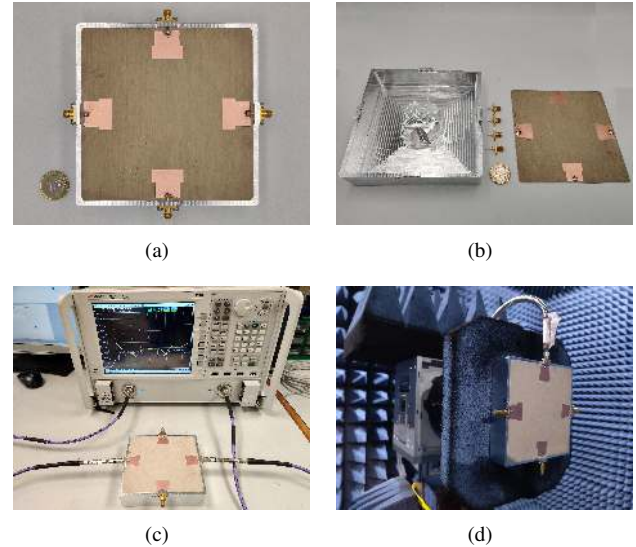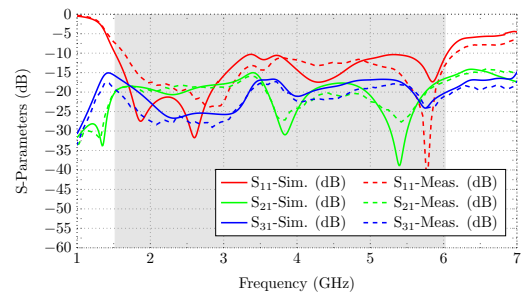
VI. FINAL DESIGN. RESULTS AND FABRICATION

The final design includes an X-shaped isolating block and a Rogers R04003C PCB (ϵ_r=3.55, $\tan\delta$=0.0027 and thickness t=0.6 mm) containing the 4 monopoles (Fig. 8(a)) which leans on top of the cavity. The inclusion of the PCB is proposed to support the 4 monopoles that facilitate the fabrication process with negligible impact on the operation frequency. The PCB is included in all the measured and simulated results of the final design.

The cavity and the isolating block have been milled from an aluminum piece and the PCB has been placed on top. Lastly, four coaxial ports have been attached to each side of the cavity, welding the inner conductor to each monopole. In Fig. 8(b) the final design is disassembled to correctly identify all the components included in the design. The antenna has been measured with a network analyzer (Fig. 8(c)) and in an anechoic chamber (Fig. 8(d)). All the results are detailed below.

Fig.9 presents the simulated (solid curves) and measured

Ref.	BW (GHz)	BW (%)	Size (mm^3)	Isolation (dB)	Indep. Ports	T.Efficiency (%)
[2]	0.70-0.96	31	220×220×100	19	2	NA
	1.7-3	55.3				
	3.3-3.8	14				
[4]	3.14-3.83	19.8	79.6×79.6×10	20	2	NA
	4.4-5.02	13.2				
[6]	1.68-4.15	84.73	180×180×2.7	30	3	85
[7]	0.8-0.96	22	220×220×42	18	2	NA
	1.7-2.7	71.8				
[8]	3.3-5	41	150×150×10	16.5	4	84
Prop.	**1.55-6**	**118**	**129.5×129.5×28.2**	**16**	**4**	**84**

TABLE 4: Comparison Table

f=1.6 GHz   (a)
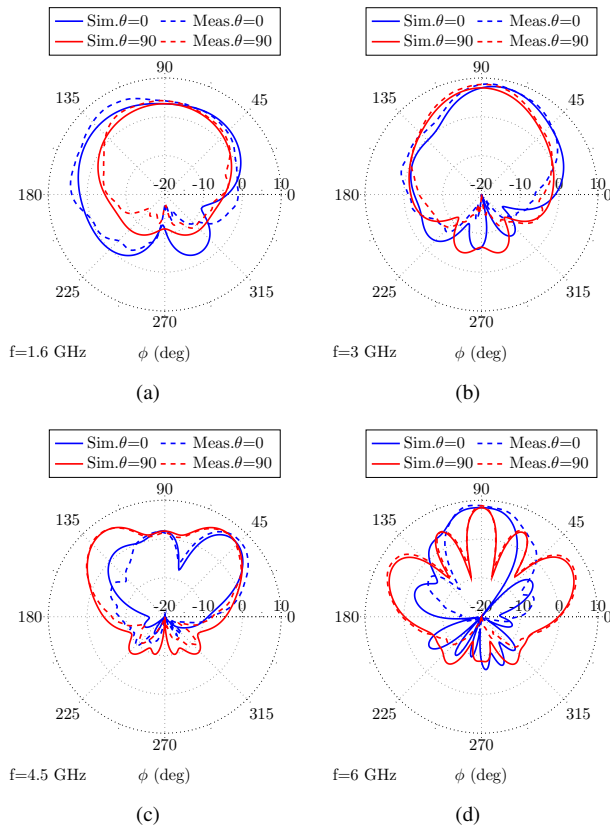
f=3 GHz   (b)

f=4.5 GHz   (c)

f=6 GHz   (d)

FIGURE 10: Simulated (solid) and Measured (dashed) radiation pattern when Port P3 is excited. Plane $\theta = 0°$ (blue) and $\theta = 90°$ (red) at: a) f=1.6 GHz, b) 3 GHz, c) 4.5 GHz and d) 6 GHz.
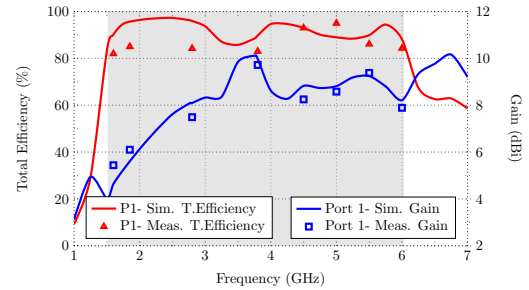

FIGURE 11: a) Total Efficiency (red-left axis) and Gain (blue-right axis) of port P1. Grey area (operating band 1.55-6 GHz)

10(a)), 3 GHz (Fig. 10(b)), 4.5 GHz (Fig. 10(c)) and 6 GHz (Fig. 10(d)). At low frequencies, the radiation pattern presents a single lobe and as the frequency increases, side lobes appear. As observed, the antenna has unidirectional pattern at the whole operating band with good agreement between simulated and measured results.

In Fig. 11 the simulated and measured total efficiency curves are represented. Total efficiency values are higher than 84% for simulated results and higher than 81% for measured results. The total efficiency (ϵ_t) is calculated as $\epsilon_t = G_r/D$ where G_r is the realized Gain and D the Directivity.

To sum up, Table 4 compares the features of the most relevant recent publications of indoor base station antennas and the proposed design, highlighting the impedance bandwidth, the size, the isolation, the number of independent ports and the total efficiency. As observed, the proposed design shows wider bandwidth than the one proposed in [8], which is an early access article from IEEE Transactions on Antennas and Propagation, obtaining similar features with a comparable size.

VII. MIMO SYSTEM

In this section, the effect of the propagation channel is studied with the evaluation of the proposed antenna in a 4×4 MIMO system. The first analysis addresses the calculation of the channel capacity in presence of mutual coupling, as proposed in [30]. The second analysis studies the envelope correlation coefficient (ECC) in different propagation conditions modeled by several angular distributions (uniform, Gaussian and

(dashed curves) S-parameters of the final design. Results confirm the wide-band behaviour, with good matching from 1.55 GHz to 6 GHz with a slight difference between simulated and measured S_{11} due to fabrication tolerances. Regarding the measured isolation, it is higher than 16 dB in all the band (see S_{21} and S_{31}). Measured isolation is slightly higher than simulated. Unlike the initial design (Fig. 1(b)), the desired minimum isolation level between ports of 15 dB is achieved.

Fig. 10 depicts measured and simulated radiation patterns in XZ plane ($\theta=0°$) and YZ plane ($\theta=90°$) at 1.5 GHz (Fig.
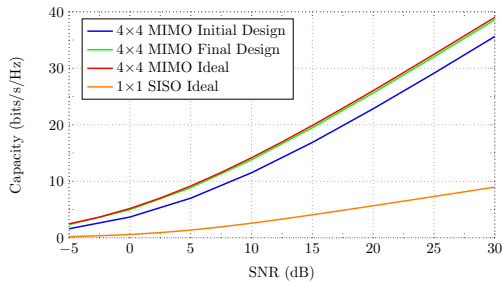
FIGURE 12: Channel Capacity.

Laplacian).

A. CHANNEL CAPACITY

Mutual coupling degrades the performance of a MIMO system [30] and one of the main concerns of this article was to increase the isolation between ports of the initial design, specially at low frequencies. In order to quantify the improvement regarding the propagation channel when the isolation is increased, the channel capacity is calculated for the initial and final design at 1.8 GHz (lowest isolation level for the initial design).

For the calculation, the procedure detailed in [30] is followed but in this case, 4 uncorrelated antennas are settled as transmitting antennas, and the 4 receiving antennas are those of the proposed design. It is assumed that the receiver has perfect channel state information (CSI) but the transmitter does not. Furthermore, the analysis is calculated in an isotropic scattering environment. With these assumptions, the ergodic capacity can be calculated using (4) [30], where I is the 4×4 identity matrix, $\overline{\gamma}_0$ the reference SNR, R the correlation matrix of receive antenna and H_w the spatially white MIMO channel with independent and identically distributed (i.i.d) complex Gaussian entries. H_w^H denotes hermitian of H_w.

$$ C = E \left\{ \log_2 \left[\det \left(I + \frac{\overline{\gamma}_0}{2} R H_w H_w^H \right) \right] \right\} \quad (4) $$

Fig. 12 represents the capacity calculated for 100000 simulated channel realizations of a 4×4 MIMO system, setting as receiving antennas the initial design (blue curve), the final design (green curve) and an ideal receiver (red curve). In addition, the capacity of an ideal 1×1 SISO systems (orange curve) is calculated for the sake of comparison. The results show an average 3 b/s/Hz increase between the initial design and the final design. The final design provides results close to the ideal 4×4 MIMO system. It can also be observed that the 4×4 MIMO capacities are in average 4 times higher than the ideal 1×1 SISO system capacities.
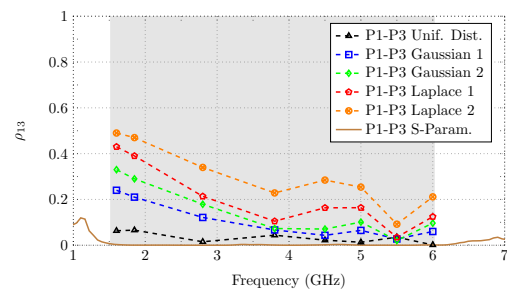
B. ENVELOPE CORRELATION COEFFICIENT (ECC)

The envelope correlation coefficient (ECC) has become a standard parameter for measuring the performance of an antenna in a MIMO system. This parameter takes into account both the propagation conditions and the radiation pattern of the antenna, and can be defined as (5) [30]. Generally, it is
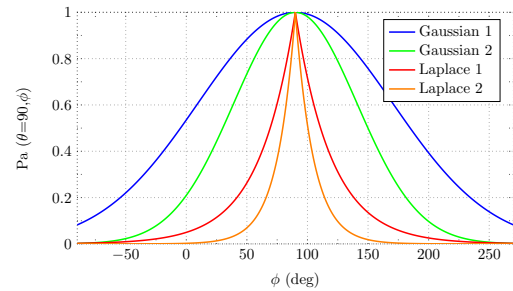
(a)
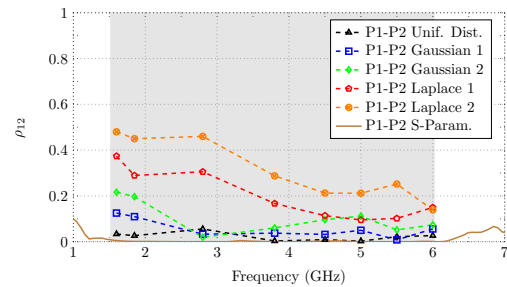
(b)

(c)

FIGURE 13: a) Analyzed angular distributions: Gaussian 1 (6), Gaussian 2 (7), Laplace 1 (8) and Laplace 2 (9) . b) ECC between P1 and P2 and c) ECC between P1 and P3.

considered a low correlation level when the ECC is lower than 0.5 [13].

$$ \rho = \frac{\iint\limits_{4\pi} g_1^H(\Omega) Pa(\Omega) g_2(\Omega)\, d\Omega}{\sqrt{\iint\limits_{4\pi} g_1^H(\Omega) Pa(\Omega) g_1(\Omega)\, d\Omega \cdot \iint\limits_{4\pi} g_2^H(\Omega) Pa(\Omega) g_2(\Omega)\, d\Omega}} $$

$$(5)$$

Regarding equation (5), $g_1(\Omega)$ and $g_2(\Omega)$ describes the two analyzed radiation patterns, where the superscript ^{H} denotes Hermitian, $\Omega = (\theta, \phi)$ is the solid angle of arrival and $Pa(\Omega)$ denotes the dyadic power angular spectrum of the incident field which is described by different angular distributions [31]. Usually, the ECC is calculated in ideal scenarios with isotropic scattering, hence $Pa(\theta,\phi)$ is assumed to be described by an uniform distribution ($Pa(\theta,\phi)=1$).

In this article, different $Pa(\theta,\phi)$ are considered for the simulation of different propagation conditions. The analyzed

distributions are depicted in Fig. 13(a) including uniform ($Pa(\theta,\phi)=1$), Gaussian (6)(7) and Laplace (8)(9) distributions. For their comparison and for simplicity, all the distributions exhibit their maximum at $\phi° = 90°$ and $\theta° = 90°$.

$$Pa(\theta,\phi) = e^{(-(\theta-\pi/2)/(\pi/10)-(\phi-\pi/2)/(\pi/5))/10} \quad (6)$$

$$Pa(\theta,\phi) = e^{(-(\theta-\pi/2)/(\pi/10)-(\phi-\pi/2))/(\pi/5))/4} \quad (7)$$

$$Pa(\theta,\phi) = e^{-|\theta-\pi/2|/(\pi/8)-|\phi-\pi/2|/(\pi/4)} \quad (8)$$

$$Pa(\theta,\phi) = e^{-|\theta-\pi/2|/(\pi/16)-|\phi-\pi/2|/(\pi/8)} \quad (9)$$

In addition, the ECC is also calculated with an approximation using the S-parameters of the antenna (10) [32] under the assumption of isotropic scattering scenario.

$$\rho = \frac{|S_{11}^* S_{12} + S_{21}^* S_{22}|^2}{(1-(|S_{11}|^2+|S_{21}|^2))(1-(|S_{22}|^2+|S_{12}|^2))} \quad (10)$$

Fig. 13(b) depicts the results of the ECC between P1 and P2 calculated with (5) using the 3D measured radiation patterns and the distributions represented in Fig. 13(a). Furthermore, the ECC is calculated with the measured S-parameters (10) and also added in Fig. 13(b). Fig. 13(c) represents the same analysis for P1 and P3. All the obtained correlation coefficients show an ECC<0.5. The best performance is obtained with the uniform distribution, followed by the Gaussian and the most complex scenario is the one modeled with the Laplace distribution. It can be observed that the narrower the distribution is, the higher the higher the correlation coefficient is.

Due to the symmetry of the antenna, the analysis of the ECC between P1-P2 and P1-P3 is enough for confirming uncorrelated radiation patterns and a good performance of the proposed 4-port antenna in different simulated propagation conditions.

VIII. CONCLUSION

In this paper, a four-port wide-band antenna with unidirectional and independent radiation patterns is presented for MIMO indoor base station applications. Measurements and simulations show impedance bandwidth (S$_{11}$ < -10 dB) of 118 % (1.55-6 GHz), total efficiency higher than 84%, isolation between ports higher than 16 dB, and ECC lower than 0.5 in different propagation conditions, providing compatibility with a 4×4 MIMO system. The antenna has dimensions of 129.5×129.5×28.2 mm^3 and provides four independent ports in such a limited space due to the use of an isolating block that increases from 10.5 dB to 16 dB the isolation between adjacent ports. Furthermore, the design does not precise differential feeding which needs the use of hybrid couplers or baluns for obtaining independent patterns and limits the number of independent ports. This feature turns this

antenna into an easy manufacturing and reasonable low-cost solution.

For the design of the isolating block, a novel methodology based on CMA has been used for identifying the nature of the coupling between ports. Decomposing the total currents and fields into modal currents and modal fields has provided valuable information to identify the mode (J_4) contributing to the coupling.

The antenna has been fabricated milling the cavity in an aluminum block and placing a Rogers PCB on top of the cavity, exhibiting good agreement between simulated and measured results. The proposed design is a proper candidate to be installed as a sub-6 GHz 5G indoor base station antenna because of its simple structure, compact size, and wide impedance bandwidth. Moreover, MIMO operation is also possible with the proposed design as it includes 4 well isolated ports with independent radiation patterns and low ECC.

REFERENCES

[1] M. Agiwal, A. Roy, and N. Saxena, "Next generation 5G wireless networks: A comprehensive survey," IEEE Communications Surveys & Tutorials, vol. 18, no. 3, pp. 1617–1655, 2016.

[2] A. Alieldin, Y. Huang, S. J. Boyes, M. Stanley, S. D. Joseph, Q. Hua, and D. Lei, "A triple-band dual-polarized indoor base station antenna for 2G, 3G, 4G and sub-6 GHz 5G applications," IEEE Access, vol. 6, pp. 49 209–49 216, 2018.

[3] Q. Hua, Y. Huang, C. Song, M. O. Akinsolu, B. Liu, T. Jia, Q. Xu, and A. Alieldin, "A novel compact quadruple-band indoor base station antenna for 2G/3G/4G/5G systems," IEEE Access, vol. 7, pp. 151 350–151 358, 2019.

[4] Q. Liu, H. Liu, W. He, and S. He, "A low-profile dual-band dual-polarized antenna with an amc reflector for 5G communications," IEEE Access, vol. 8, pp. 24 072–24 080, 2020.

[5] Z.-Y. Zhang, G. Fu, W.-J. Wu, J. Lei, and S.-X. Gong, "A wideband dual-sleeve monopole antenna for indoor base station application," IEEE antennas and wireless propagation letters, vol. 10, pp. 45–48, 2011.

[6] S. X. Ta, D. M. Nguyen, K. K. Nguyen, C. Dao-Ngoc, and N. Nguyen-Trong, "A tripolarized antenna with ultra-wide operational bandwidth," IEEE Transactions on Antennas and Propagation, 2020.

[7] Y. Zhao, C. Rakluea, T. Hongnara, and S. Chaimool, "A compact dual-broadband multiple-input multiple-output (MIMO) indoor base station antenna for 2G/3G/LTE systems," IEEE Access, vol. 7, pp. 82 238–82 245, 2019.

[8] K.-L. Wong, J.-Z. Chen, and W.-Y. Li, "Four-port wideband annular-ring patch antenna generating four decoupled waves for 5G multi-input-multi-output access points," IEEE Transactions on Antennas and Propagation, 2020.

[9] J. Molins-Benlliure, A. Llanga-Vargas, D. K. Park, M. Ferrando-Bataller, and M. Cabedo-Fabrés, "MIMO antenna for indoor low-band 5G base stations," in 2019 IEEE International Symposium on Antennas and Propagation and USNC-URSI Radio Science Meeting. IEEE, 2019, pp. 151–152.

[10] J.-N. Hwang and S.-J. Chung, "Isolation enhancement between two packed antennas with coupling element," IEEE Antennas and wireless propagation letters, vol. 10, pp. 1263–1266, 2011.

[11] M. Singh and M. S. Parihar, "A compact 4×4 MIMO antenna with high isolation for 5G application," in 2019 IEEE Asia-Pacific Microwave Conference (APMC). IEEE, 2019, pp. 688–690.

[12] Z. Tang, J. Liu, R. Lian, Y. Li, and Y. Yin, "Wideband differentially fed dual-polarized planar antenna and its array with high common-mode suppression," IEEE Transactions on Antennas and Propagation, vol. 67, no. 1, pp. 131–139, 2018.

[13] M.-Y. Li, Y.-L. Ban, Z.-Q. Xu, G. Wu, K. Kang, Z.-F. Yu et al., "Eight-port orthogonally dual-polarized antenna array for 5G smartphone applications," IEEE Transactions on Antennas and Propagation, vol. 64, no. 9, pp. 3820–3830, 2016.

[14] M.-Y. Li, Y.-L. Ban, Z.-Q. Xu, J. Guo, and Z.-F. Yu, "Tri-polarized 12-antenna MIMO array for future 5G smartphone applications," IEEE Access, vol. 6, pp. 6160–6170, 2017.

[15] H. Jin, L. Zhu, H. Zou, Y. Luo, S. Xu, and G. Yang, "A wideband dual-polarized antenna and its array with electrically downtilt function for 5G sub-6 GHz communication applications," IEEE Access, vol. 8, pp. 7672–7681, 2019.

[16] H. Huang, Y. Liu, and S. Gong, "A broadband dual-polarized base station antenna with sturdy construction," IEEE Antennas and Wireless Propagation Letters, vol. 16, pp. 665–668, 2016.

[17] S. Fu, Z. Cao, X. Quan, and C. Xu, "A broadband dual-polarized notched-band antenna for 2/3/4/5G base station," IEEE Antennas and Wireless Propagation Letters, vol. 19, no. 1, pp. 69–73, 2019.

[18] L. Zhao, L. K. Yeung, and K.-L. Wu, "A coupled resonator decoupling network for two-element compact antenna arrays in mobile terminals," IEEE Transactions on Antennas and Propagation, vol. 62, no. 5, pp. 2767–2776, 2014.

[19] H. Piao, Y. Jin, and L. Qu, "A compact and straightforward self-decoupled MIMO antenna system for 5G applications," IEEE Access, vol. 8, pp. 129 236–129 245, 2020.

[20] Z. Ren, A. Zhao, and S. Wu, "MIMO antenna with compact decoupled antenna pairs for 5G mobile terminals," IEEE Antennas and Wireless Propagation Letters, vol. 18, no. 7, pp. 1367–1371, 2019.

[21] A. Zhao and Z. Ren, "Size reduction of self-isolated MIMO antenna system for 5G mobile phone applications," IEEE Antennas and Wireless Propagation Letters, vol. 18, no. 1, pp. 152–156, 2018.

[22] M. Cabedo-Fabres, E. Antonino-Daviu, A. Valero-Nogueira, and M. F. Bataller, "The theory of characteristic modes revisited: A contribution to the design of antennas for modern applications," IEEE Antennas and Propagation Magazine, vol. 49, no. 5, pp. 52–68, 2007.

[23] H. Li, Z. T. Miers, and B. K. Lau, "Design of orthogonal MIMO handset antennas based on characteristic mode manipulation at frequency bands below 1 GHz," IEEE Transactions on Antennas and Propagation, vol. 62, no. 5, pp. 2756–2766, 2014.

[24] A. Araghi and G. Dadashzadeh, "Oriented design of an antenna for MIMO applications using theory of characteristic modes," IEEE Antennas and Wireless Propagation Letters, vol. 11, pp. 1040–1043, 2012.

[25] D.-W. Kim and S. Nam, "Systematic design of a multiport MIMO antenna with bilateral symmetry based on characteristic mode analysis," IEEE Transactions on Antennas and Propagation, vol. 66, no. 3, pp. 1076–1085, 2017.

[26] J. Dong, S. Wang, and J. Mo, "Design of a twelve-port MIMO antenna system for multi-mode 4G/5G smartphone applications based on characteristic mode analysis," IEEE Access, vol. 8, pp. 90 751–90 759, 2020.

[27] R. Harrington and J. Mautz, "Theory of characteristic modes for conducting bodies," IEEE Transactions on Antennas and Propagation, vol. 19, no. 5, pp. 622–628, 1971.

[28] Harrington, R and Mautz, J, "Computation of characteristic modes for conducting bodies," IEEE Transactions on Antennas and Propagation, vol. 19, no. 5, pp. 629–639, 1971.

[29] M. Cabedo Fabres, "Systematic design of antennas using the theory of characteristic modes," Ph.D. dissertation, 2008.

[30] X. Chen, S. Zhang, and Q. Li, "A review of mutual coupling in MIMO systems," IEEE Access, vol. 6, pp. 24 706–24 719, 2018.

[31] B. T. Quist and M. A. Jensen, "Optimal antenna radiation characteristics for diversity and MIMO systems," IEEE Transactions on Antennas and Propagation, vol. 57, no. 11, pp. 3474–3481, 2009.

[32] S. Blanch, J. Romeu, and I. Corbella, "Exact representation of antenna system diversity performance from input parameter description," Electronics letters, vol. 39, no. 9, pp. 705–707, 2003.

JAIME MOLINS-BENLLIURE was born in València, Spain in 1990. He received the bachelor's degree in Telecommunications Technology and Services Engineering in 2015 and the master's degree in Telecommunications Engineering in 2017 at the Polytechnic University of Valencia (UPV), València, Spain. He studied his last master's degree and wrote his thesis under an Erasmus scholarship in Karlsruhe Institute of Technology (KIT), Karslruhe, Germany.

He was involved in a 5G antenna research project Financed by Huawei Technologies OY Finland designing and fabricating antennas for 5G MIMO communication systems. He is currently pursuing the Ph.D. degree in telecommunication engineering with the Instituto de Telecomunicaciones y Aplicaciones Multimedia (iTEAM) at the Polytechnic University of Valencia (UPV) under a scholarship supported by the Spanish Ministry of Science and Innovation. He has submitted several articles in international and national conferences for the European Conference on Antennas and Propagation (EuCAP) and for the International Symposium on Antennas and Propagation and North American Radio Science Meeting (IEEE APS/URSI). His research interests focus on the analysis and the design of IoT/5G antennas for new generation devices with the use of new materials.

EVA ANTONINO-DAVIU (M'00) was born in Valencia, Spain, in 1978. She received her M.S. and Ph.D. degrees in electrical engineering from Universitat Politècnica de València, Valencia, Spain, in 2002 and 2008, respectively. In 2005, she joined the Communications Department at Universitat Politècnica de València as Assistant Professor, and in 2012 she became Associate Professor at this University. In 2005 she joined the Institute of Telecommunications and Multimedia Applications (iTEAM), where she became Vice-Director of Research in 2016. In 2005 she stayed as a guest researcher at the Department of Antennas & EM Modelling of IMST (Kamp-Lintfort, Germany), at the Laboratory of Electronics, Antennas and Telecommunications (LEAT) of the University of Nice Sophia-Antipolis (France) in 2018, and at the ATHENA Group of the Georgia Institute of Technology (Atlanta, GA, USA) in 2019. Her current research interests include characteristic modes, small antennas, wideband and multi-band antenna design, and antenna design for MIMO, IoT and mm-wave applications. Eva Antonino-Daviu has published more than 200 papers in renowned journals and conferences in the field of antennas and propagation, as well as 2 book chapters. Eva Antonino-Daviu is Associate Editor of IEEE Antennas and Propagation Magazine and since 2018 she leads the EurAAP working group on Small Antennas Eva Antonino was the recipient of 2019 IEEE AP-S Lot Shafai Mid-Career Distinguished Achievement Award, for her contribution to the systematic design of antenna systems for practical applications using characteristic modes and promoting access of women to engineering.

MARTA CABEDO-FABRÉS was born in Valencia, Spain, in 1976. She received the M.S. and Ph.D. degrees in Telecommunication Engineering from the Universitat Politècnica de València (UPV), Spain, in 2001 and 2007, respectively. In 2001, she joined the Electromagnetic Radiation Group, UPV, as Research Assistant. In 2004, she became an Associate Professor with the Communications Department, UPV. She has also been Vice-Director of Quality and Accreditation at Telecommunication Engineering Faculty since 2015. Her current scientific interests include numerical methods for solving electromagnetic problems, and design and optimization techniques for wideband and multi-band antennas.

MIGUEL FERRANDO-BATALLER was born in Alcoy, Spain, in 1954. He received the M.Sc. (Ing.) and Ph.D. (Doctor Eng.) degrees in electrical engineering (telecommunication engineering) from the Technical University of Catalonia (UPC), Barcelona, Spain, in 1977 and 1982, respectively. He has been Research Asistant (1977) and Associate Professor (1982), with the Antennas, Microwave, and Radar Group, Communications Department, Telecommunication Engineering School, UPC. In 1990, he joined the Universitat Politècnica de València, UPV, Valencia, Spain, where he is currently a Full Professor and leader of Antenna and Propagation Lab . From 1991 to 1996, he was the Director of the Telecommunication Engineering School, UPV. From 1996 to 1999 and from 2005 to 2009, he was UPV Vice-rector for academic planning and information and communication technologies. From 2009 to 2013 he was Director of the Lifelong Learning Center at UPV.

He has authored more than 200 technical papers, conference publications and book chapters in specialized volumes. His current research interests include antennas, electromagnetic scattering, numerical methods, antenna design and e-learning activities.

. . .